



# Unsteady aerodynamic characteristics and dynamic performance of high-speed trains during plate braking under crosswind

Dazhou Lv · Yong Liu · Qiyao Zheng · Lin Zhang · Jiqiang Niu 

Received: 9 September 2022 / Accepted: 17 May 2023 / Published online: 30 May 2023  
© The Author(s), under exclusive licence to Springer Nature B.V. 2023

**Abstract** The braking system of a train, which is one of its key technologies, plays a vital role in ensuring the safe operation of the train. Plate braking can be used as a method for braking of a high-speed train during an emergency; the higher the train speed, the better the braking effect. In this study, dynamic grid technology is used to simulate plate movement, and the IDDES with the SST k- $\omega$  turbulence model is used to simulate the unsteady aerodynamic characteristics of the train during the plate braking process. The aerodynamic force and torque obtained from the fluid simulation are then fed as an external load into the simplified center of the multibody system dynamics model of the high-speed train. Finally, the safety indices of the plate-braking train under crosswinds of different speeds are obtained. The results show that the rapid opening of the plate provides a large braking force to the train but destabilizes the flow field around and especially above it; this phenomenon is further aggravated by crosswinds. The aerodynamic force distribution of each car in the train is considerably changed by the crosswind, and the proportion of lateral force acting on the head car significantly increases.

The aerodynamic forces acting on each car further increase due to the opening of the plate. From the perspective of vehicle dynamics performance, an increase in the crosswind speed leads to noticeable increases in the derailment coefficient and wheel load reduction rate of each car; derailment and overturn may also occur. Under crosswind, the head car presents the worst dynamic performance, which is further deteriorated by the opening of the plate. The impact of the tail car is relatively small. The dynamic performance of the head car can thus be used to evaluate train safety. As a precaution, the plate of the head car should never be opened during strong crosswinds.

**Keywords** High-speed train · Plate braking · Crosswind · Aerodynamic performance · Dynamic performance

## 1 Introduction

As train operations continue to improve, braking technologies face increasingly severe challenges. To ensure the safe braking of high-speed trains, a new technology called plate braking has been applied; however, this is still in its experimental stage. High-speed trains travel at high speeds and are light in weight, but they have poor overturning resistance and

---

D. Lv · Y. Liu · Q. Zheng · J. Niu (✉)  
School of Mechanical Engineering, Southwest Jiaotong  
University, Chengdu 610031, China  
e-mail: jiqiang\_niu@163.com

L. Zhang · J. Niu  
Graduate School of Tangshan, Southwest Jiaotong  
University, Tangshan 063000, China

are seriously affected by crosswinds. Under crosswind, the opening of the plate braking system causes severe deterioration of the lateral aerodynamic performance of the train, and the train shakes violently, thus negatively affecting its operational safety and riding comfort. The safe operation of plate-braking trains is thus restricted by the deterioration of its lateral aerodynamic performance under complex and variable crosswinds along the railway.

A study on plate-braking trains was recently conducted in Japan [1]. Different types of plate-braking devices were installed on various magnetic levitation (maglev) test trains, and several line tests were conducted. The braking plate effect in the tunnel was found to be good, and the braking deceleration reached 0.2 g [2]. Researchers at Tongji University successfully developed a new braking plate device and adapted it on a train to carry out line tests. The effect of plate braking at the high-speed stage was obvious [3–5]. Through simulations and full-scale tests, researchers found that the shape of the plate has little effect on braking [6]; however, it has an impact on the lateral aerodynamic performance of the train, and maintaining the plate shape consistent with the top surface of the train may be the best decision. Considering the mechanical structure and flow field changes, researchers found that a reasonable plate opening angle is approximately  $75^\circ$  [7, 8], arranging a series of plates on the train roof produces a better effect than arranging a single plate with equal area [9], and the car-connection part is an ideal location for arranging the plates. Placing a single large plate downstream of the car-connection produces a better effect than setting a single large plate upstream of the car-connection [10, 11]. The location of the air conditioner and pantograph should also be considered when deciding the layout of the plates [12]; placing two adjacent plates too close to each other will cause interference [13, 14]. When plates are arranged in series, aerodynamic drag is the largest for the first plate, while it is lower for the downstream plates [15]. During a wind tunnel test, Takami [16] found that opening the plate within 0.2 s resulted in an impulse change of the aerodynamic drag. Zhai et al. [17] also found that a rapid opening of the plate produces violent fluctuations in the surrounding pressure field, forming pressure pulses; the aerodynamic drag of the plate in this case also undergoes pulse changes, which are further aggravated by crosswind.

Railway lines are widely distributed across environments that are prone to change, especially in strong crosswind zones, which can easily degrade the aerodynamic performance of the train [18–20]. An effective method to prevent the impact of crosswinds on trains is setting a wind barrier [21–23]. However, the transition section appears in the wind barrier owing to the complex terrain along the railway line, causing sudden changes in the flow field around the railway line and affecting the driving safety of the train [24–27]. Current research on train operational safety is conducted by combining computational fluid dynamics (CFD) and vehicle system dynamics [28–30]. Some of these studies have focused on the design of the transition section of the wind barrier to improve the safety and comfort of trains passing through it [31]. By changing the flow field around the train using body surface flow control technology, improvements in the lateral aerodynamic performance of the train can be achieved [32].

Studies on the unsteady aerodynamic and dynamic performances of a train during plate opening under crosswind have rarely been conducted. Research on plate braking safety is urgently required. The scientific aim of this study is to: (1) reveal the evolution law of the flow field around a train during plate opening under crosswind, (2) explore the impact mechanism of crosswind on the unsteady aerodynamic performance and dynamic characteristics of the train, and (3) obtain the safety index of the train at different crosswind speeds in combination with the vehicle dynamics model to improve plate braking safety under crosswind. This study is structured as follows. Section 1 provides a brief introduction to the study of aerodynamic plate braking. The governing equations of the fluids and geometric models of CFD are presented in Sect. 2. The numerical settings, including calculation methods, computational domain, meshing method, and setup for the solution, are explained in Sect. 3. The models and settings for the vehicle spatial-coupling dynamics (VSD) are included in Sect. 4. Verification of the numerical settings used in this study is presented in Sect. 5. In Sect. 6, the unsteady aerodynamic and flow field changes of a train and its plates under different crosswinds are analyzed alongside the dynamic performance of trains equipped with brake plates. Finally, the important conclusions and future prospects of this study are presented in Sect. 7.

## 2 Aerodynamics methodology

### 2.1 Fluid governing equations

Governing equations for fluid flow include the continuity equation (law of conservation of mass), momentum equation (law of conservation of momentum), and energy equation (law of conservation of energy, also known as the Navier–Stokes equation). For this study, the travelling speed of the modeled high-speed train is 97.2 m/s. This corresponds to a Mach number of less than 0.3 for the flow; thus, an incompressible air model was adopted in the train external flow field, and the Navier–Stokes equation is expressed as follows:

$$\frac{\partial u_i}{\partial x_i} = 0 \tag{1}$$

$$\frac{\partial u_i}{\partial t} + u_j \frac{\partial u_i}{\partial x_j} = -\frac{\partial p}{\rho \partial x_i} + \frac{\mu \partial^2 u_i}{\rho \partial x_i \partial x_j} \tag{2}$$

where  $x_i$  and  $x_j$  are the different spatial coordinate components;  $u_i$  and  $u_j$  are the velocity components of the fluid in the  $x$ ,  $y$ , and  $z$  directions;  $\rho$  is the air density of the flow field;  $p$  is the flow field pressure, and  $\mu$  the aerodynamic viscosity.

### 2.2 Geometric models

The CRH train model, simplified according to the EN standard [33], is comprised of two streamlined cars and one middle car, as shown in Fig. 1a. The total length of the train is 79 m, and the lengths of the head/tail car and middle car are 26.5 m and 25 m, respectively. The spacing between adjacent cars is 0.5 m. Four plates (1st, 2nd, 3rd, and 4th) are located on the train roof, and the distance between adjacent plates is approximately

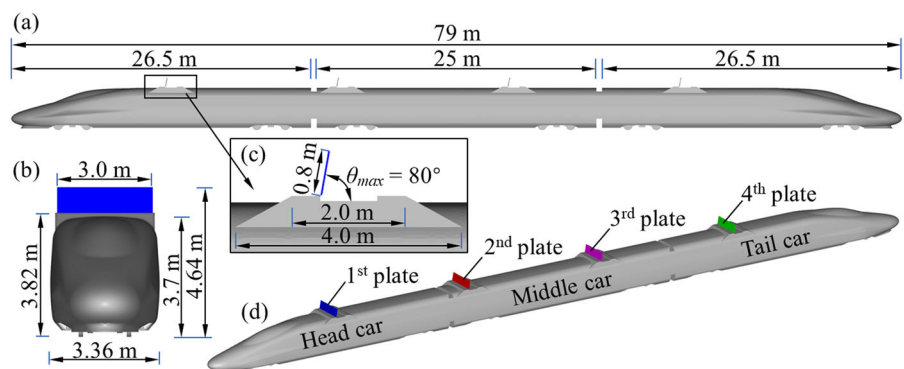
15 m, considering the flow interaction between adjacent plates [3, 5]. The width of the train is 3.36 m, and the heights of the train when the plate is closed and fully opened are 3.82 m and 4.64 m, respectively, as shown in Fig. 1b. These measures meet the requirements of the railway construction gauge. The main dimensions of the plate and its base are shown in Fig. 1c: the length and width of the plate are 0.8 m and 3.0 m, respectively, and the maximum opening angle ( $\theta_{max}$ ) of the plate is  $80^\circ$  [8]. A three-dimensional (3D) view of the train with a fully opened plate is shown in Fig. 1d.

## 3 Numerical settings for CFD

### 3.1 Calculation method

In this study, the flow field around the train has a large separation and strong unsteady flow. Different turbulence models have different requirements for the grid resolution and calculation accuracy. Currently, there are three methods for the simulation of unsteady flow fields: unsteady Reynolds-averaged Navier–Stokes (URANS), large-eddy simulation (LES), and detached-eddy simulation (DES). Each method has advantages and disadvantages. URANS is often used in engineering fields that require low grid resolutions and few calculation resources. However, it has a limited calculation accuracy, and does not easily capture certain detail flows, especially the unsteady, large separation, and inverse-pressure gradient flows involved in this study. The LES method describes small-scale turbulent flows well, but it requires a high grid resolution and large computational times. As a hybrid algorithm, the DES method combines the advantages of both the LES and URANS methods. The

**Fig. 1** Main dimensions of the full-scale model of the train with braking plates: **a** side view, **b** front view, **c** local view of the plate and its base, and **d** 3D view



LES method is used in the separation area, and the URANS method is automatically adjusted for the remaining areas. This is a reliable and efficient method for the 3D unsteady turbulent flow simulations of trains. When the grid arrangement near the wall is not realistic, the boundary layer region is solved using the LES model instead of the URANS equation, leading to a model stress distribution (MSD) loss [34]. Delayed detached-eddy simulation (DDES) solves the MSD issue by modifying the feature length, but its calculation leads to an unreasonable distribution of the flow field and a “logarithmic layer mismatch” [35]. To solve these issues, the improved delayed detached-eddy simulation (IDDES) method was proposed in 2012 [36], which was proven in previous studies [37–40]. The IDDES method is widely used in the simulation of vehicle aerodynamics [41–48]. The current study includes a detailed analysis of the flow field around a train. The airflow separation around the braking plates and the development of a vortex structure provide important flow field information. To capture the flow separation more accurately, the IDDES method based on SST  $k-\omega$  is used to simulate the unsteady flow field around the plate-braking train under different crosswinds.

The turbulent kinetic energy equation and specific dissipation rate equation of the SST  $k-\omega$  model are given by Eqs. (3) and (4), respectively:

$$\rho \frac{Dk}{Dt} + \rho \frac{\partial(ku_i)}{\partial x_i} = \frac{\partial}{\partial x_j} \left( T_k \frac{\partial k}{\partial x_j} \right) + G_k - Y_k \quad (3)$$

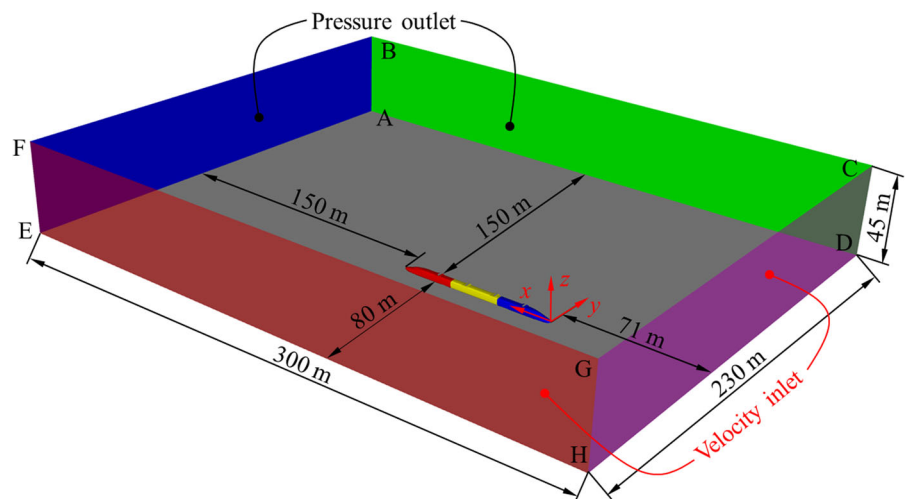
$$\rho \frac{D\omega}{Dt} + \rho \frac{\partial(\omega u_i)}{\partial x_i} = \frac{\partial}{\partial x_j} \left( T_\omega \frac{\partial \omega}{\partial x_j} \right) + G_\omega - Y_\omega + D_\omega \quad (4)$$

where  $G_k$  is the turbulent kinetic energy generated by the laminar velocity gradient,  $G_\omega$  is the turbulent kinetic energy generated by the  $\omega$  equation,  $T_k$  and  $T_\omega$  are the diffusivities of  $k$  and  $\omega$ , respectively,  $Y_k$  and  $Y_\omega$  are the turbulence caused by the diffusion of fluids, and  $D_\omega$  is the orthogonally divergent term.

### 3.2 Computational domain

Reasonable dimensions and boundary definitions of the computational domain are the basis for obtaining reliable calculation results. The length, width, and height of the full-scale computational domain adopted in this study are 300, 230, and 45 m, respectively, as shown in Fig. 2. The train runs in the negative direction along the  $x$ -axis. To simulate the aerodynamic performance of the train under crosswind, both the end face (CDHG) in front of the train and one side face (EFGH) on the computational domain are defined as the speed inlet boundary; whereas the other two sides of the computational domain (ABCD and ABFE) and the upper surface are set as the pressure outlet boundary; the lower face (ADHE) of the computational domain is defined as the static sliding wall boundary with the sliding speed being the same as the train travelling speed. The boundaries of the computational domain are sufficiently distant from the train to avoid their influence on the flow field around it. The distance between the speed inlet boundary (CDHG) at

**Fig. 2** Dimensions of the full-scale computational domain for the train with plates under crosswind



the front of the train and the train itself is set at 71 m, and the crosswind speed inlet boundary (EFGH) is located 80 m away from the train. The distance between the outlet boundaries (ABCD and ABFE) and the train is 150 m, meeting the requirements of the EN standard [33]. The velocity inlet boundary is defined by the velocity specification method of components, which is adopted to deal with the inlet velocity; the velocity values in the  $x$ - and  $y$ -directions correspond to the train and crosswind speeds, respectively. In this study, the train speed ( $U_{\text{train}}$ ) was set at 97.2 m/s, and the tested crosswind speeds ( $U_{\text{wind}}$ ) were 0, 10, 15, and 20 m/s. The turbulent conditions at the inlet and outlet boundaries are described by  $k$  and  $\omega$ , respectively, according to Eqs. (5) and (6), respectively:

$$k = \frac{3(IU_{\text{ref}})^2}{2} \quad (5)$$

$$\omega = \frac{k^{1/2}}{0.07HC^{1/4}} \quad (6)$$

$$U_{\text{ref}} = \sqrt{U_{\text{train}}^2 + U_{\text{wind}}^2} \quad (7)$$

where  $I$  is the turbulent intensity of the incoming flow (0.1%),  $U_{\text{ref}}$  is the resulting velocity,  $U_{\text{train}}$  and  $U_{\text{wind}}$  are the train and wind velocities, respectively,  $H$  is the characteristic length of the train (the height of the train of 3.7 m), and  $C$  is an empirical constant ( $C = 0.09$ ).

### 3.3 Meshing method

Dynamic grid technology was used to simulate the plate opening. Considering the large movement range of the plate, this is bound to cause a large deformation of the grid during its reconstruction: the calculation resources required would be very high, calculation efficiency would be significantly reduced, and poor quality grids would be obtained, further reducing the calculation accuracy. To circumvent this problem, the regions close to each plate were isolated from the computational domain, forming four independent computational domains. The grid changes of the small computational subdomains, including the plates, do not interfere with the large computational domain of the train. The overlapping boundaries between the four small computational domains and the large computational domain are defined as the interface boundary to

exchange flow information between these computational domains. Using these methods, a local grid was reconstructed, reducing the scale of grid reconstruction and improving the computational efficiency.

The dynamic grid technology in Fluent is only applicable to tetrahedral grids. Thus, the computational domains where the plates are located are divided into tetrahedral grids. The size of grid  $L_{M1}$  on the surface of the plate was approximately 3 mm, and the outermost grid ( $L_{M3}$ ) size was approximately 20 mm. The large computational domain was meshed using the SnappyHexMesh file in OpenFOAM. Two refinement regions (Refinementbox-1 and Refinementbox-2) were set around the train and plates, ensuring a good grid resolution of the region considered in this study. This also improves the simulation accuracy of the flow field around the train, as shown in Fig. 3a. The size of grid  $L_{M2}$  on the surface of the vehicle body was approximately 5 mm. Boundary layer grids were added to improve the simulation accuracy of the flow field near the wall; the thickness  $\sigma_1$  of the layer closest to the wall was 0.1 mm. A total of five layers and a transition factor of 1.2 are obtained, as shown in Fig. 3b.

### 3.4 Setup for solution

The pressure-based solver of Fluent was used to solve all calculations in this study. The SIMPLE algorithm was adopted to deal with the coupling relationship between the velocity and pressure. Both the convection and dissipation terms were discretized using second-order schemes. An implicit second-order accuracy scheme was applied for time-stepping in the time domains, with a time step of 0.0002 s; each time step had a total of 30 iterations. Finally, the residuals of each equation converged to below  $10^{-5}$  for each time step. The braking plate is the emergency device of the train to stop; hence, it needs to respond quickly [16]. The opening time  $t_p$  of the braking plate in this study is set to be fast, at 0.2 s, as shown in Fig. 4. To prevent damage to the mechanical structure, the rotation speed  $\omega_p$  of the plate is small at the start and finish of the opening process.

While running, the fluid acting on the train produces an aerodynamic drag ( $F_x$ ), aerodynamic lateral force ( $F_y$ ), and aerodynamic lift ( $F_z$ ) along the  $x$ -,  $y$ - and  $z$ -directions, respectively. The aerodynamic force also produces torque, and the moments

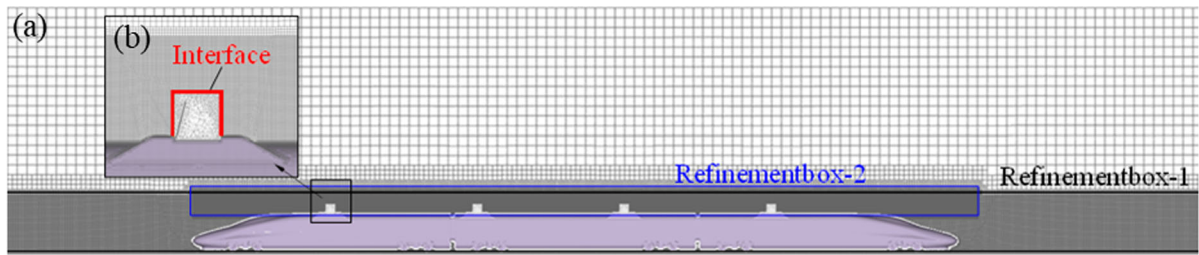


**Fig. 3** Mesh distribution around the calculation mode: **a** mesh along the symmetry plane of the train and **b** mesh around the braking plate

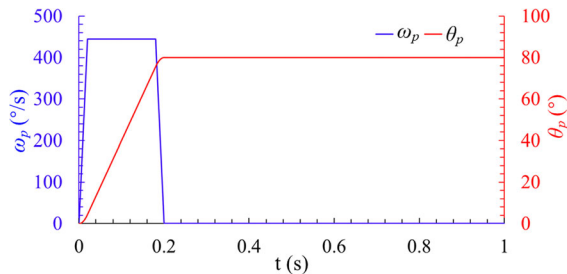


**Fig. 4** Time history of the opening angle  $\theta_p$  and rating velocity  $\omega_p$  of the plate

decomposed into the three directions  $x$ -,  $y$ - and  $z$ - are rolling ( $M_{xi}$ ), nodding ( $M_{yi}$ ), and yawing ( $M_{zi}$ ) moments, respectively. The geometric center of each part is selected as the extraction center of the aerodynamic torque, where the geometric center position of the tail car is the same as that of the head car, as shown in Fig. 5.

## 4 Models and settings for VSD

### 4.1 Vehicle model

The neural network method [49, 50] or dynamic simulation [51, 52] is generally used for dynamics analysis. Neural networks require a large amount of experimental data and can accurately describe nonlinear phenomena, such as convective mechanics and classical mechanics [53]. Dynamic simulation is more commonly used for train dynamics analysis, due to its speed and high precision. This study therefore favored the dynamic simulation method. The VSD model is established using the multibody dynamics software SIMPACK, which is based on an engineering prototype of a high-speed train. The following parts are simplified to facilitate the VSD modeling calculation:

- (1) The wheelset, frame, vehicle body, and axle box are all regarded as rigid bodies. No elastic deformation is considered.
- (2) Vehicle excitation is caused only by track irregularity. No influence from the track elastic deformation is considered.
- (3) The wheelset has a rim that is constantly in contact with the rail in the vertical direction.
- (4) The wheel rail creep is considered based on a method by Kalker's creep theory. The wheel rail friction coefficient considered is 0.4.

Each vehicle was composed of one body, two frames, eight axle boxes, and four wheelsets. Each component of the body, frame, and wheelset had six degrees of freedom (DOF). The axle box considered only the rotational DOFs around the wheelset. The DOF of the vehicle system is shown in Table 1, where  $X$ ,  $Y$ ,  $Z$ ,  $\theta$ ,  $\varphi$ , and  $\psi$  are the longitudinal, transverse, and vertical displacements of the train along the  $x$ -,  $y$ - and  $z$ -axis and the rolling, nodding, and yawing motions of the train rotating around the  $x$ -,  $y$ - and  $z$ -axis, respectively; the subscripts  $c$ ,  $b_i$ ,  $w_j$ , and  $a_k$  represent the car body,  $i$ th frame,  $j$ th wheelset, and  $k$ th axle box, respectively.

The single-car topological relationship of the VSD model is obtained according to the aforementioned DOFs, as shown in Fig. 6. The single-stage suspension system, two-stage suspension system, and wheel-rail contact forces in the model are simplified as a spring-damping structure. The air springs are simulated by the Spring-Damper Parallel Cmp; the characteristics of the primary vertical shock absorber and the secondary lateral shock absorber are simulated using the Spring-Damper Serial PtP; and the anti-hunting shock absorber is simulated with the Force/Torque by  $u(t)$  PtP. The nonlinear treatment [54, 55] of the suspension system is illustrated in Fig. 7.

**Fig. 5** Extraction center of the aerodynamic torque

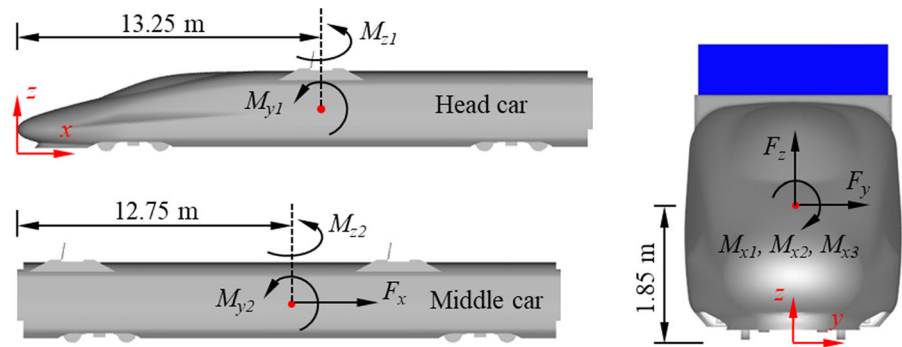


**Table 1** Degrees of freedom of the vehicle system

Component	x	y	z	Roll	Pitch	Yaw	Remarks
Car body	$X_c$	$Y_c$	$Z_c$	$\theta_c$	$\varphi_c$	$\psi_c$	-
Framework	$X_{bi}$	$Y_{bi}$	$Z_{bi}$	$\theta_{bi}$	$\varphi_{bi}$	$\psi_{bi}$	$i = 1 \sim 2$
Wheelset	$X_{wj}$	$Y_{wj}$	$Z_{wj}$	$\theta_{wj}$	$\varphi_{wj}$	$\psi_{wj}$	$j = 1 \sim 4$
Axle box	-	-	-	-	$\varphi_{ak}$	-	$k = 1 \sim 8$

4.2 Main parameters and settings

To ensure the integrity of the vehicle system and reliability of the simulation results, the VSD model was simplified and its main parameters determined, as shown in Table 2.

In this study, the train speed is set at 350 km/h. The measured excitation of the Wuhan-Guangzhou section of the Beijing-Guangzhou high-speed railway line is selected as the input for track irregularity. The aerodynamic force and torque obtained from the fluid simulation are loaded into the simplified center of each car in the VSD model as an external load. This is a common method used in the dynamic research of high-speed trains under crosswinds [56, 57]. The loading center of each aerodynamic load is shown in Fig. 5. Different aerodynamic loading times  $t_a$  have different impacts on the simulation results; when it is above 2.0 s, its influence can be ignored. Hence, the loading time selected for each working condition was 2.0 s. The length of the track in the simulation was set to 1 km. Under the effect of aerodynamic drag, the speed change of the train within 2.0 s does not exceed 5 km/h; therefore, the train speed throughout the entire simulation process was considered to be constant.

4.3 Evaluation index

The stability of train operation was evaluated using indicators, such as the derailment coefficient, rate of wheel load reduction, lateral wheelset force, and lateral stability. Safety of train operation was a key concern of this study. Thus, evaluating the performance of plate braking, used in emergency braking, is of great importance. This was achieved by looking at whether the derailment coefficient [58] and rate of wheel load reduction [59] met their specified requirements [60]. According to the design code of the high-speed railway in China [61], the limit values for the rate of wheel load reduction,  $\Delta P/\bar{P}$ , and derailment coefficient,  $Q_y/P_z$ , are both 0.8, as shown in Eqs. (8) and (9), respectively.

$$\Delta P/\bar{P} \leq 0.8, U_{\text{train}} > 160\text{km/h} \tag{8}$$

$$\frac{Q_y}{P_z} \leq 0.8, R > 400\text{m} \tag{9}$$

where  $\Delta P$  is the reduction in the wheel load,  $\bar{P}$  is the average static axial load of each wheelset,  $Q_y$  and  $P_z$  are the lateral and vertical forces, respectively, acting on the rail by the wheel on the climbing rail side, and  $R$  is the radius of curvature of the orbit.

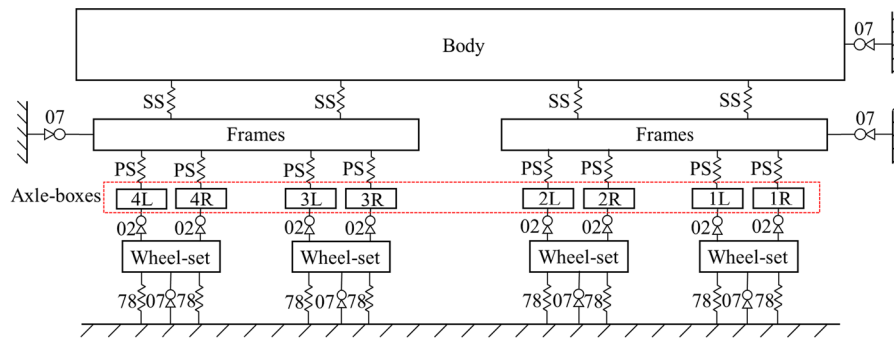
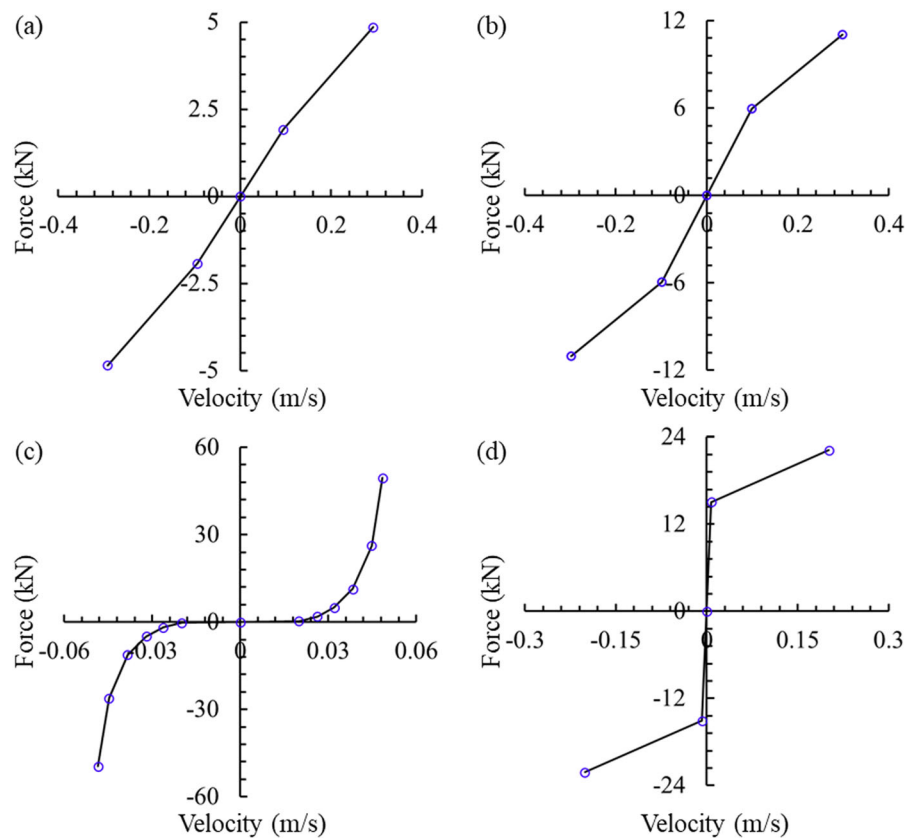


**Fig. 6** Schematic diagram of the topological relation in the VSD model

**Fig. 7** Nonlinear suspension system of the train: **a** primary vertical shock absorber, **b** secondary lateral shock absorber, **c** secondary lateral stop, and **d** anti-snake shock absorber



**5 Verification of the numerical settings in CFD**

The model used by Takami [16] to simulate a wind tunnel is consistent with that adopted in this study, including the calculation conditions. For this reason, the same model was selected for numerical verification, with the following characteristics: the length of the closed and test sections of the wind tunnel test were 6.5 m and 7 m, respectively; dimensions of the wind

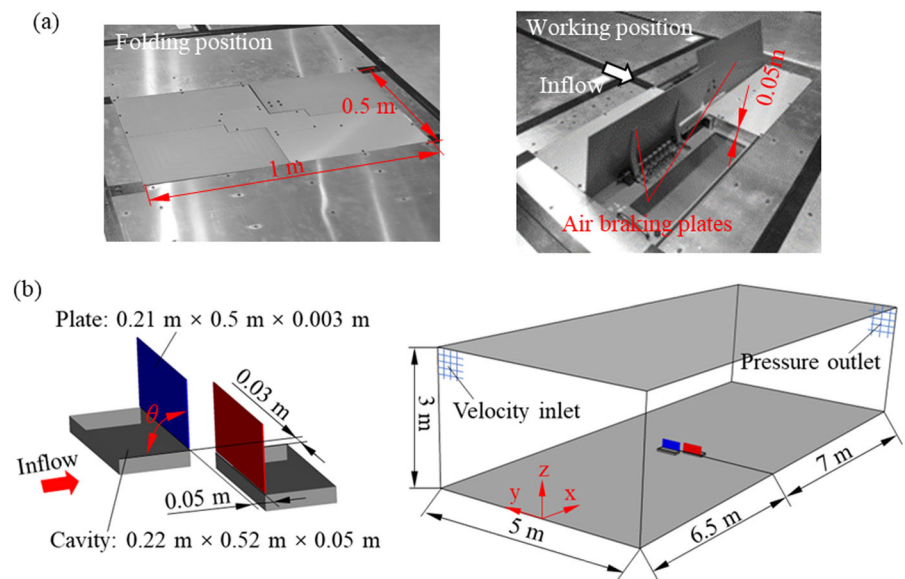
tunnel were 3.0 m × 5.0 m (height × width); wind speed of the incoming airflow was 83.3 m/s; dimensions of the braking plate were 0.5 m × 0.21 m × 0.003 m; dimensions of the cavity were 0.504 m × 0.214 m × 0.05 m; opening speed of the braking plates was set to fast; empty running time from the command to the braking force reaching its average value was 0.06 s; and the maximum opening angle  $\theta$  was 90°. The aerodynamic drag of the plate was measured using load units



**Table 2** Main parameters of the dynamics model of the vehicle system

Item	Unit	Motor car	Trailer car
Vehicle spacing	mm	17,500	
Wheelbase	mm	2500	
Nominal rolling circle diameter of wheel	mm	860	
Profile of wheel	–	LMA	
Profile of rail	–	T60kg/m	
Mass of rocker type journal box	kg	48	
Mass of wheelset	kg	1750	1900
Mass of frame	kg	3125	2270
Mass of vehicle (empty)	kg	34,900	33,750
Longitudinal/vertical stiffness of Tumber journal box node	kN/m	13,700	
Transverse stiffness of Tumber journal box node	kN/m	5500	
Longitudinal/transverse stiffness of primary steel spring	kN/m	985	
Vertical stiffness of primary steel spring	kN/m	1170	
Longitudinal/transverse stiffness of secondary air spring	kN/m	169	167
Vertical stiffness of secondary air spring	kN/m	300	278

**Fig. 8** Dimensions and location of the models in: **a** the wind tunnel experiment and **b** simulation



CLS-2KNB (rated load: 2 kN). A model of the braking plate device for the wind tunnel test is shown in Fig. 8a. More detailed information on the wind tunnel tests and its settings can be found in the mentioned study [16]. The method, numerical settings, and grid generation methodology introduced in Sect. 3 were selected to calculate the case. The computational domain and boundary conditions for the numerical simulation are shown in Fig. 8b. The distances between the braking plates and the velocity inlet and pressure outlet were 6.5 m and 7 m, respectively.

The drag force first increases and then decreases with the increase of the opening angle of the plate, reaching its maximum value for an opening angle of 75°, as shown in Fig. 9. The simulated time history curve of the aerodynamic drag is in agreement with the results obtained experimentally. The error deviations of the maximum and average aerodynamic drag are 3.26% and 5.32%, respectively, both being within the allowable range of 10%. The numerical algorithm used in this study, and its results, are thus considered reliable.

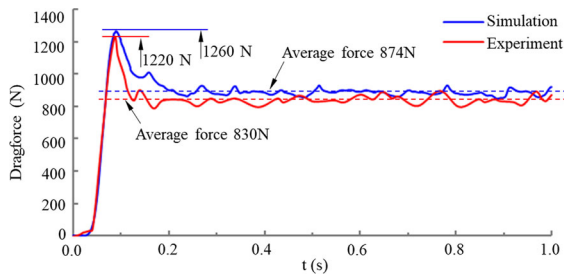


**Fig. 9** Comparison of the results from the drag force of the aerodynamic braking unit obtained in the wind tunnel experiment with those from the numerical simulation

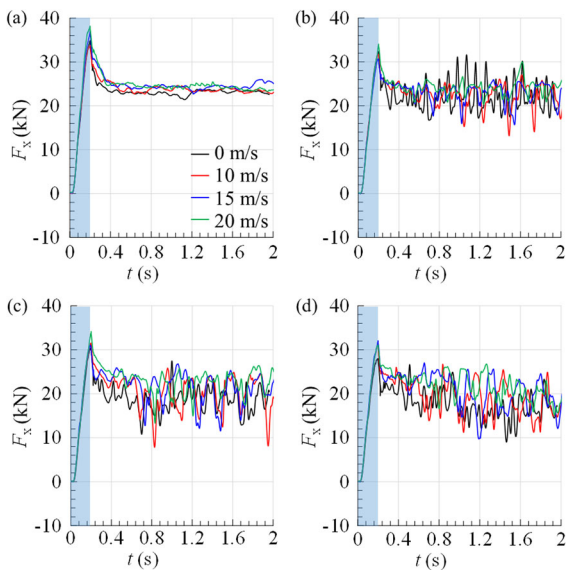


**Fig. 10** Time-history curve of the aerodynamic drag of multiple plates: (a) 1st, (b) 2nd, (c) 3rd, and (d) 4th plates

## 6 Results and analysis

### 6.1 Analysis of the aerodynamic force

The aerodynamic drag of the plates rapidly increases during the opening process of the plates, as shown in Fig. 10. After the plate movement cycle finishes, the drag of the plates decreases rapidly and tends to stabilize. For multiple plates arranged in series, the aerodynamic drag on the downstream plate is lower than that on the upstream plate. The time variation of the aerodynamic drag associated with each plate on the train roof is consistent. Nevertheless, the fluctuation of the aerodynamic drag on the 1st plate when fully opened is small, whereas its fluctuation on the downstream braking plates (2nd, 3rd, and 4th plates)

is severe; this is caused by the separation vortex of the upstream plates. A constant  $Q$  iso-surface is used to describe the transient vortex structure around the train, as shown in Fig. 11 (a detailed introduction to the  $Q$  value is given in [62]). The airflow separates at the edge of the upstream plate and forms a separation vortex. This vortex moves downstream with the airflow and impacts the downstream plates, causing obvious fluctuations in their aerodynamic force. Under the action of crosswind, the separation vortex generated on the upstream plates shifts in the direction of the crosswind. An increase in the crosswind speed leads to a reduction in the vortex impacting the downstream plate and weakening of the fluctuation of the drag on the downstream plate, which is in agreement with the time-history curve plotted in Fig. 10. An increase in the wind speed increases the peak value of the drag, which could be related to the direction of the airflow. Based on the structural development of the flow field, the following sections present further analysis and discussions.

In the opening stage of the plate, its lateral force fluctuates, as shown in Fig. 12. This is further aggravated by the crosswind. However, when the crosswind speed exceeds 15 m/s, its effect is no longer noticeable. Although the negative peak value of the lateral force of 1st plate is greater than the positive peak value, there is an inverse relationship for the other plates. Moreover, the closer the other plates are to the downstream, the higher is their positive peak value, and the lower is their negative peak value. When the movement of the plate is completed, the lateral force on it rapidly tends to zero, showing periodic fluctuations. The fluctuation of the lateral force on the 1st plate is significantly smaller than that on the other plates downstream. The crosswind speed has a limited effect on the lateral force of the plate when fully opened.

Figure 13 shows the time-history curve of the aerodynamic lift on multiple plates. The aerodynamic lift force on the plates reverses when the plates are opened. With the continuous opening of the plates, the aerodynamic lift initially increases and then decreases rapidly. When the plates are fully opened, the lift force gradually stabilizes, maintaining a certain negative lift that relates to the structure of the braking plates and development of the flow field. The aerodynamic lift of the braking plate comprises adhesion and pressure forces. The adhesion force and pressure on the upper

**Fig. 11** Top view of the transient iso-surfaces, corresponding to the Q criterion ( $Q = 3000$ ) under different crosswind speeds

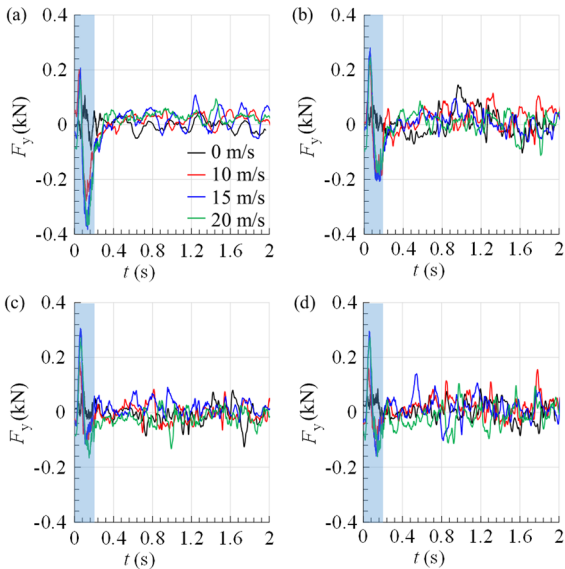
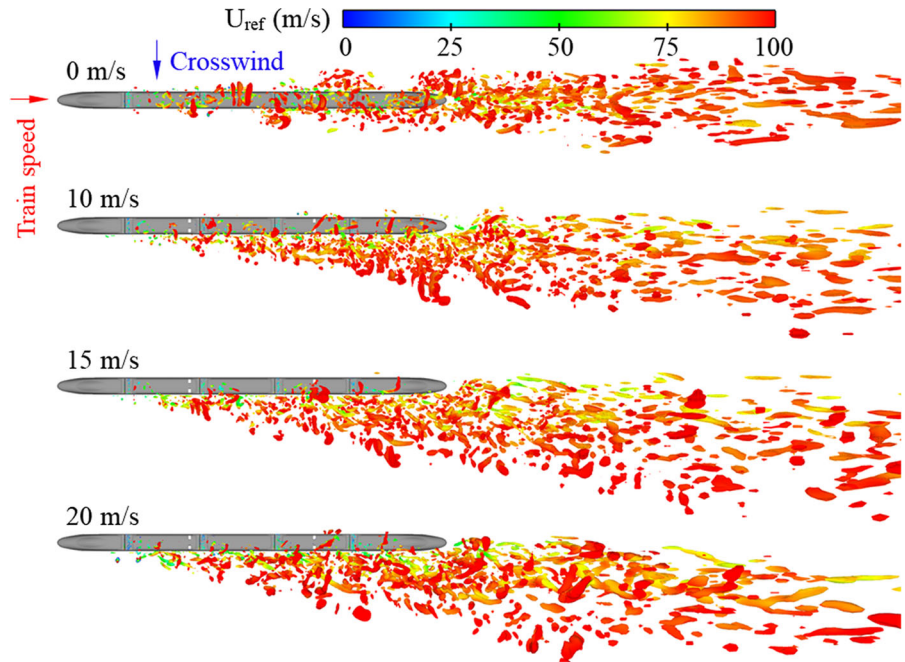


**Fig. 12** Time-history curve of the aerodynamic lateral force of multiple plates: **a** 1st, **b** 2nd, **c** 3rd, and **d** 4th plates

and lower surfaces of the braking plate are small due to its small thickness. The aerodynamic lift force is primarily determined by the vertical component  $F'_{pz1}$  of the pressure gradient force  $F_{p1}$  between the front and back of the braking plate. Each brake plate has similar lift variation trends at different crosswind speeds; thus, the flow field development during the

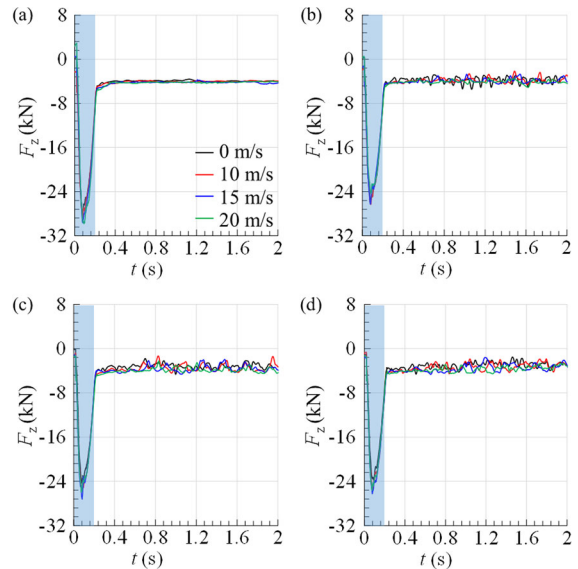
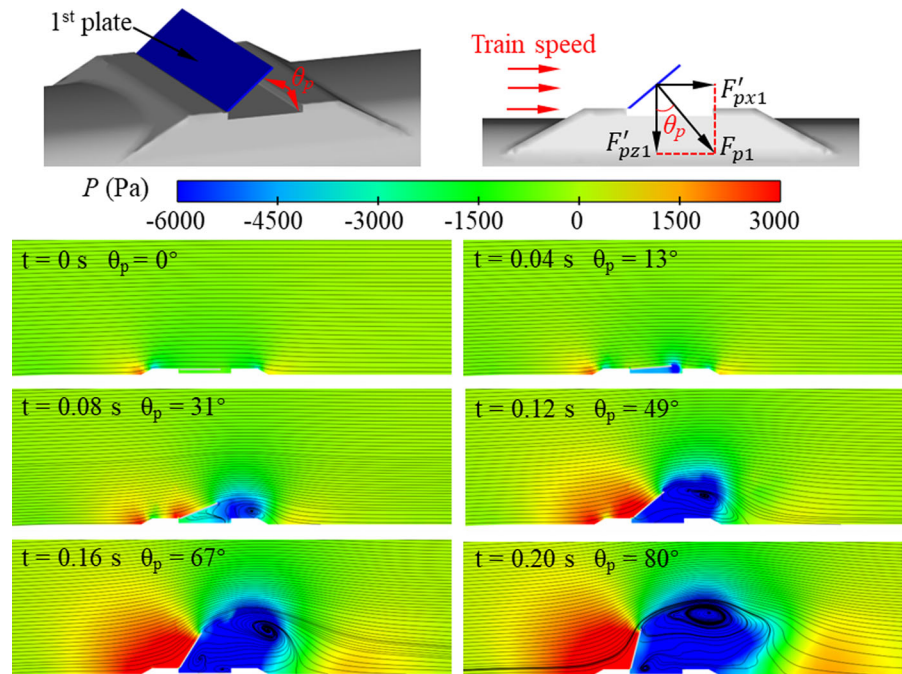


**Fig. 13** Time-history curve of the aerodynamic lift force of multiple plates: **a** 1st, **b** 2nd, **c** 3rd, and **d** 4th plates

opening process of the 1<sup>st</sup> plate when the crosswind is 10 m/s, as shown in Fig. 14, is chosen for the analysis. With the opening of the braking plate, the plate hinders the development of the incoming flow, and the airflow separates around it, forming a negative pressure region behind the plate. The pressure gradient between the front and back of the plate increases rapidly, also

**Fig. 14** Transient pressure distribution and streamlines at different opening angles along the symmetry plane of the 1st plate under a crosswind of 10 m/s



increasing the aerodynamic lift. The component of the differential pressure force  $F_{p1}$  in the vertical direction decreases when the opening angle  $\theta$  increases, leading to a decrease in the aerodynamic lift. The separation vortex impacts the aerodynamic lift force on each downstream plate, which fluctuates significantly after stabilization, in a similar manner to the fluctuation of the aerodynamic drag. The differences in the aerodynamic lift peak value under different crosswind speeds are less than 10%, indicating that the crosswind has little effect on the aerodynamic lift of the plate.

The aerodynamic drag on the head car body increases rapidly during the process of plate opening without crosswind, as shown in Fig. 15a. When the plates open fully, their drag continues to increase, reaching a plateau at which it remains stable. The amplitude of the aerodynamic drag on the head car body, while the board opens, decreases significantly under crosswind. When the plates are fully opened, the drag on the body decreases with the increase in the crosswind speed; this is because the crosswind changes the pressure distribution around the head car. The pressure on the leeward side of the head car decreases below negative under the action of the crosswind, and the pressure decreases with an increase

in the crosswind speed, as shown in Fig. 16a. More regions at the front end of the head car experience a negative pressure, leading to a reduction in the drag on the head car. The drag on the middle and tail cars rapidly increases with the opening of the braking plates and then gradually stabilizes when they are fully opened, as observed in Fig. 15b and c. The aerodynamic drag on the body of the middle and tail cars increases with an increase in the crosswind speed. The drag on the middle car, containing two braking plates, is clearly affected by the crosswind because it enhances the flow velocity, increases the pressure difference between the front and back of the braking plates, and increases the aerodynamic drag of the car body. The lateral force on each vehicle body is significantly affected by the crosswind, as shown in Fig. 15d–f. The lateral force on the head car is increased significantly owing to the crosswind. On the tail car, it is relatively insignificant; on the middle car, it fluctuates significantly, influenced by the separation vortices of the 2<sup>nd</sup> and 3<sup>rd</sup> plates. The lift force on each car body initially increases rapidly and then decreases rapidly during the opening of the braking plates, which is consistent with the lift change on the braking plates, as shown in Fig. 15g–i. The

**Fig. 15** Time-history of the aerodynamic force of each car of the high-speed train: **a, d, and g** represent the head car body in the  $x$ -,  $y$ -, and  $z$ -coordinates, respectively; **b, e, and h** represent the middle car body in the  $x$ -,  $y$ -, and  $z$ -coordinates, respectively; **c, f, and i** represent the tail car body in the  $x$ -,  $y$ -, and  $z$ -coordinates, respectively

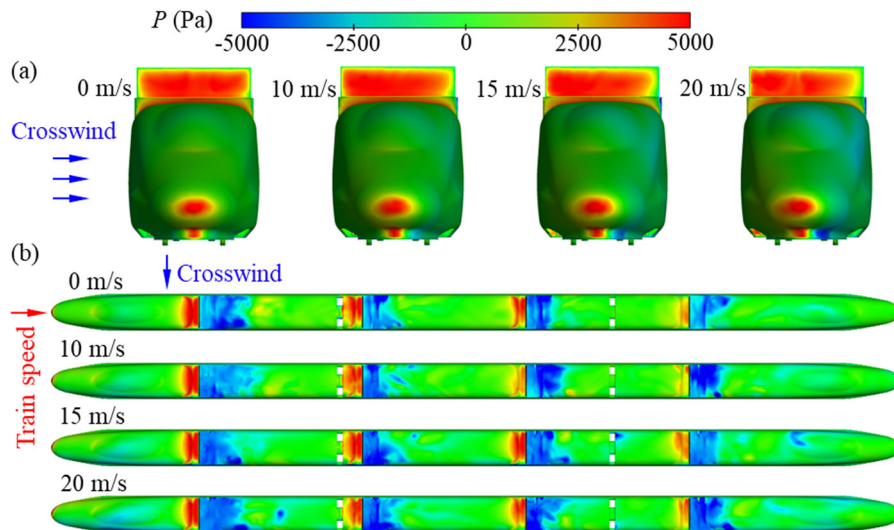
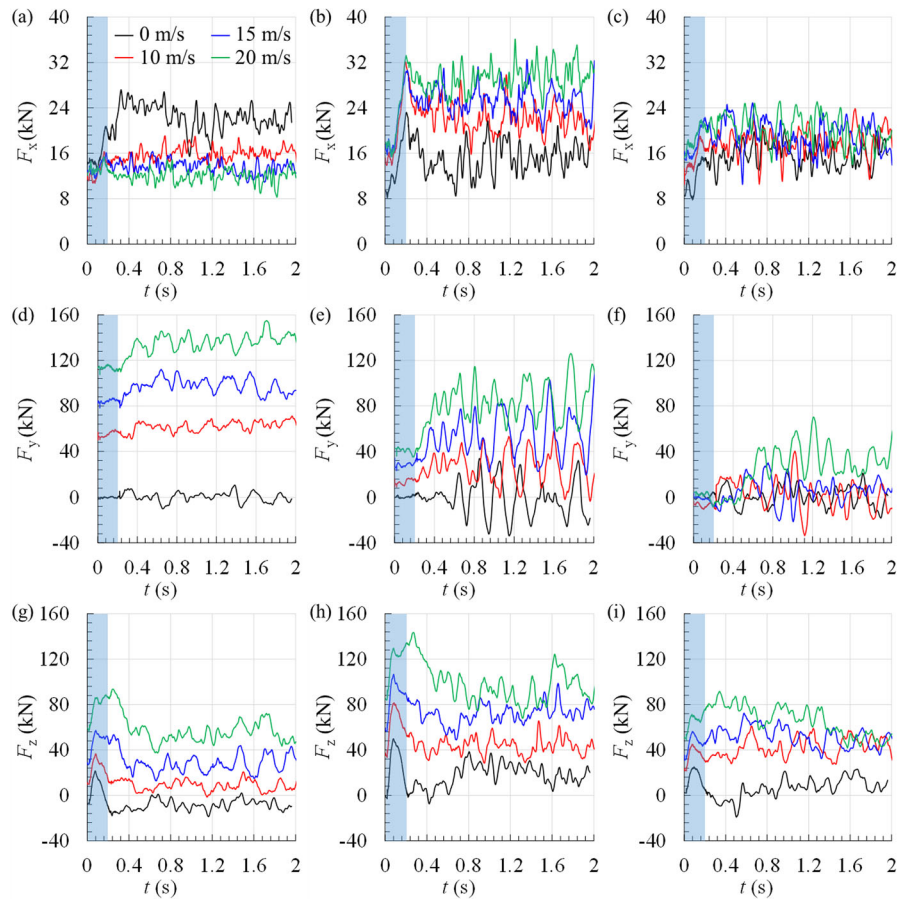


**Fig. 16** Pressure distribution across the train under different crosswinds: **a** front surface of the head car and **b** upper surface of the train

crosswind expands the negative pressure regions behind the plates distributed at the top of the train, decreasing the pressure and increasing the lift on the car body when the crosswind speeds increase, as shown in Fig. 16b.

## 6.2 Flow field characteristics of the train during plate braking under crosswind

When the crosswind speed increases, the inclination of the wake of the plates is intensified, weakening the interference between the flow fields around the adjacent plates, especially under a strong crosswind of 20 m/s, as shown in Fig. 17. The wake of the upstream plate does not influence the downstream plate, which is due to the interference of the upstream plate on the downstream plate being weakened by the crosswind. The speed of the airflow in front of the downstream plate also increases. This observation

explains the enhanced aerodynamic drag on the downstream braking plates, as shown in Fig. 10.

When the plate is not opened, its base is raised on the roof, causing local air flow to accelerate, according to Fig. 18. When the opening angle reaches  $13.3^\circ$  ( $t = 0.04$  s), the rapid opening speed of the plate and the sluggish development of the surrounding airflow prevent the flow field above the train roof to change significantly. When the opening angle of the plate reaches  $30^\circ$  ( $t = 0.08$  s), the flow field around the plate starts to gradually change, and a pair of opposite rotating asymmetric vortices appear downstream of the plate. As the opening angle continues to increase, the blockage effect of the plate on the airflow is stronger, the velocity of airflow downstream of the plate decreases significantly, and the range continues to expand. The separated airflows on both sides of the plate form a pair of separated vortices downstream of the plate, whose scale continues to increase with the

**Fig. 17** Transient streamline distribution and velocity contour across the horizontal section Z1 at a height of 4.0 m from the top surface of the rail during the opening of the plate under different crosswind speeds

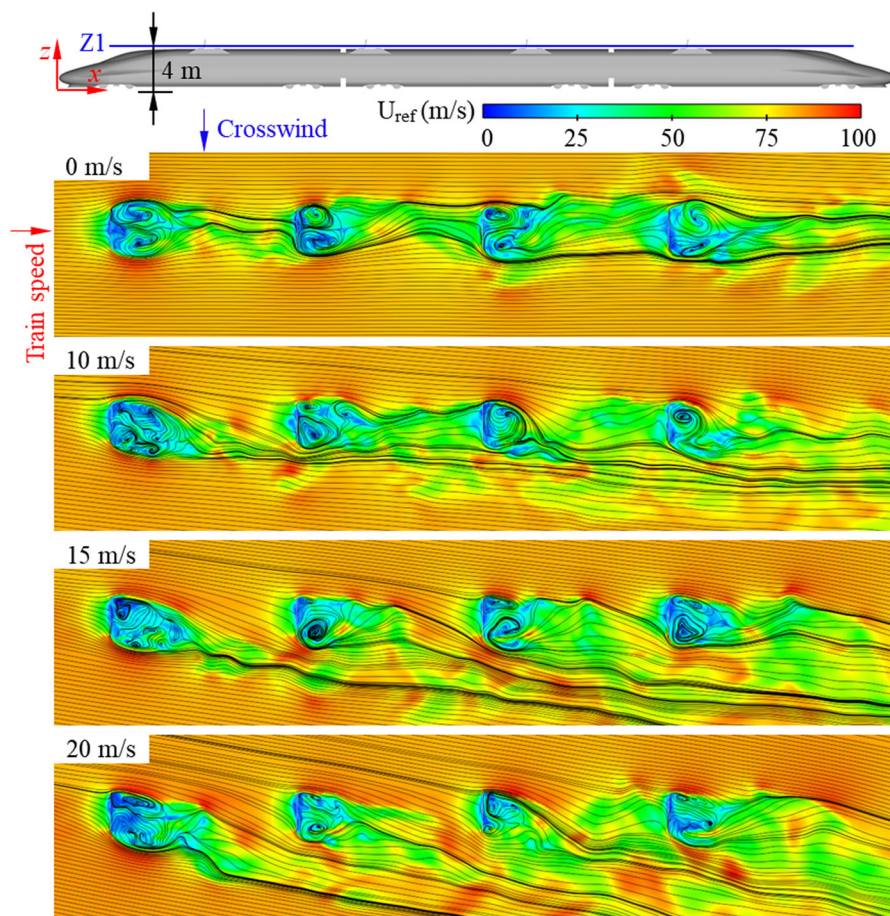
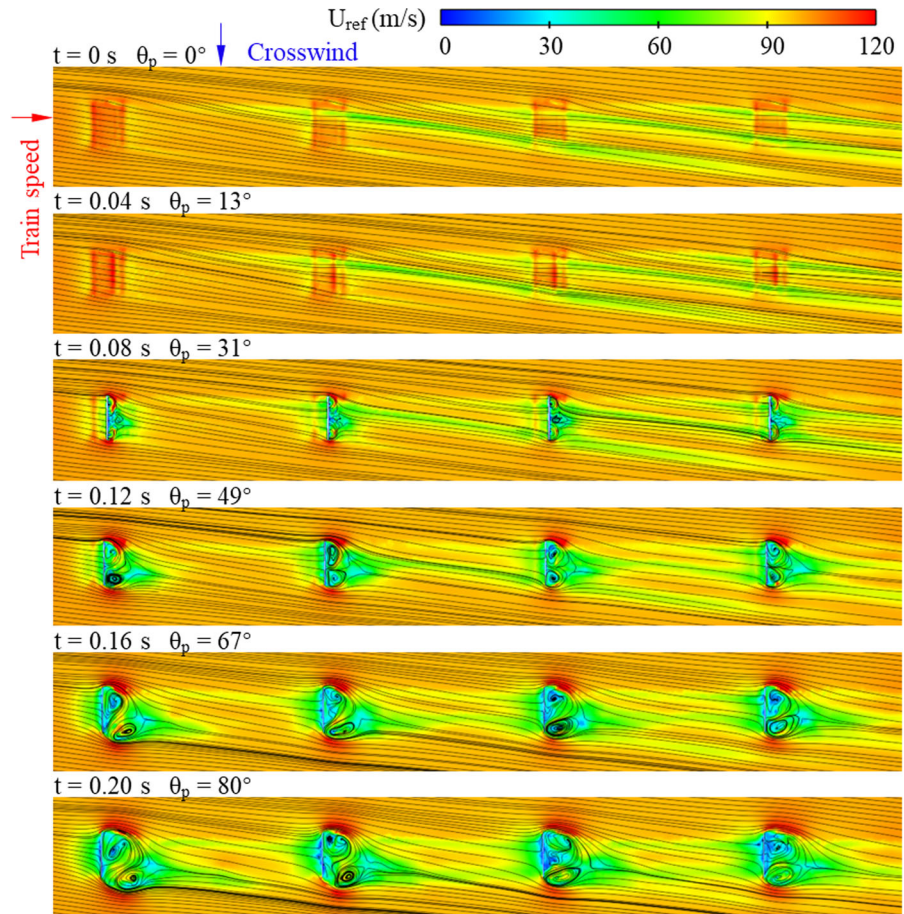


**Fig. 18** Transient streamline distribution and velocity contour across the horizontal section Z1 at a height of 4.0 m from the top surface of the rail during the opening of the plates under a crosswind of 10 m/s



increase of the opening angle of the plate. Part of the airflow in the wake of the upstream plate acts on the flow field around the downstream plate, affecting the aerodynamic performance of the downstream plate.

Crosswind causes the separation of airflow at the upper and lower surfaces of the train, forming separation vortices on the leeward side of the train that disturb the flow field, as shown in Fig. 19. The flow field on the leeward side of the train becomes more complex, and the lateral stability of the flow field around the train deteriorates progressively. The separation vortices on the leeward side of the head car at the X1 and X2 sections in the front and back of the 1<sup>st</sup> plate are small and located mainly in the train roof. A large number of vortices are distributed on the leeward side and top region of both the middle car and tail car in the X3, X4, X5, X6, X7, and X8 sections. The

asymmetric distribution of separation vortices around the train promotes the fluctuation of lateral and vertical forces on the train. This is consistent with the fluctuation degree of the lateral force and lift observed on the middle and tail cars as significantly greater than that on the head car, as shown in Fig. 15.

### 6.3 Dynamic performance of the train during plate braking under crosswind

To evaluate the train operation safety during plate braking, the derailment coefficient and rate of wheel load reduction are calculated as described in Sect. 4.3.

From Table 3, the open/close state of the plates does not affect the derailment coefficient law of the train cars, which increases with the increase of the crosswind speed. The influence of the crosswind speed on

**Fig. 19** Transient streamline distribution and velocity contour of cross sections at different distances from the train nose during the opening of the plate under different crosswind speeds

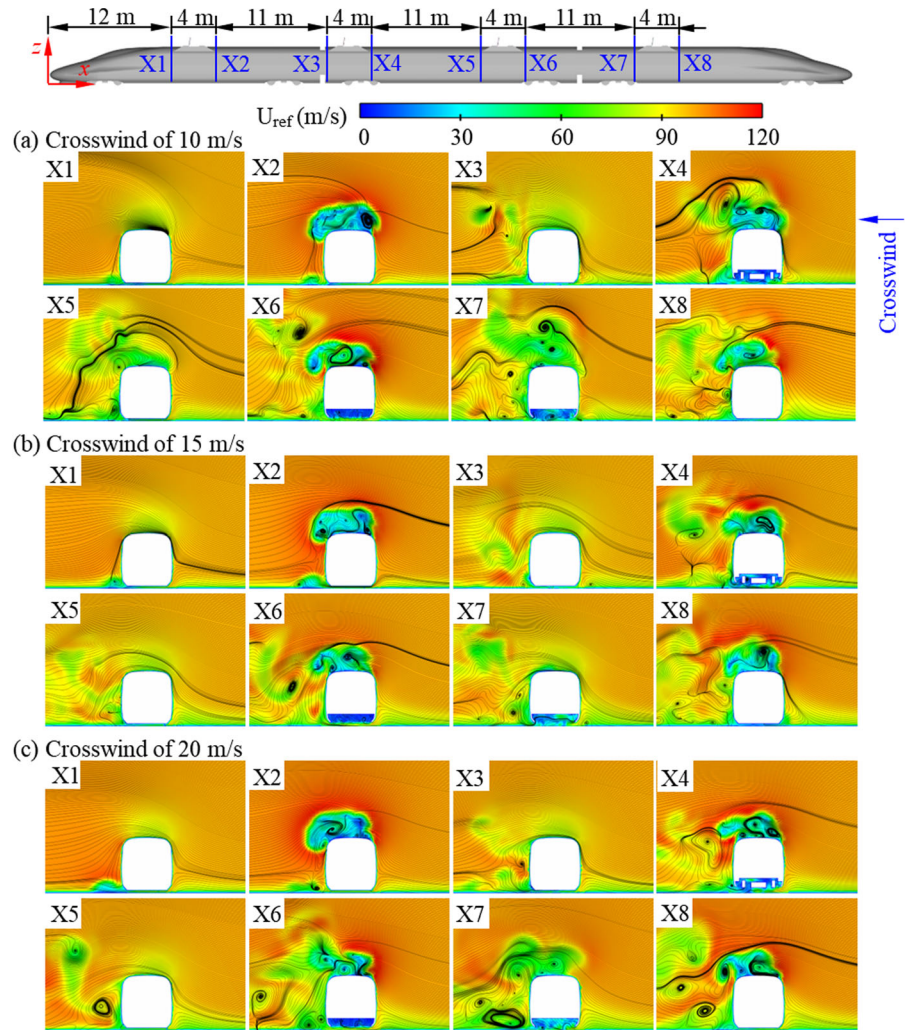


**Table 3** Derailment coefficient for each car in the plate-braking train under different crosswind speeds

Wind speed (m/s)	Head car		Middle car		Tail car	
	Closed	Opening	Closed	Opening	Closed	Opening
0	0.044	0.077	0.036	0.041	0.034	0.040
10	0.191	0.275	0.074	0.134	0.054	0.113
15	0.274	0.419	0.112	0.274	0.083	0.133
20	0.62	> 0.8	0.215	0.368	0.115	0.216

the tail car is minimal due to the small aerodynamic force on the tail car compartment and the 4<sup>th</sup> plate. However, the derailment coefficient of the tail car increases with the increase of the crosswind speed. At any crosswind speed, the derailment coefficient of the head car is always the largest and can be used to evaluate the safety of the entire train. When the plates

are opening, the derailment coefficient of each car deteriorates significantly, increasing the probability of train derailment. When the crosswind speed is lower than 15 m/s, the derailment coefficient of the train does not exceed its limit during the opening of the plate. When the crosswind speed reaches 20 m/s, the derailment coefficient of the head car before opening the



**Table 4** Rate of wheel load reduction for each car in the plate-braking train under different crosswind speeds

Wind speed (m/s)	Head car		Middle car		Tail car	
	Closed	Opening	Closed	Opening	Closed	Opening
0	0.237	0.294	0.224	0.282	0.197	0.281
10	0.465	0.694	0.241	0.427	0.119	0.208
15	0.53	> 0.8	0.341	0.765	0.201	0.315
20	> 0.8	> 0.8	0.461	> 0.8	0.218	0.474

braking plates is 0.6; although this is below the limit of 0.8, it threatens the safety of the train. When the braking plates are opened, the derailment coefficient of the head car far exceeds its limit, and the train derails. Although the derailment coefficient of the middle car increases with an increase in the crosswind speed, it remains at a relatively safe threshold (below 0.4).

Opening the plates increases the rate of wheel load reduction on each car, as shown in Table 4. Opening and closing the plates does not change the load reduction rate law of the head car or of the middle car, which increase with the increase of the crosswind speed (especially that of the head car). When the crosswind speed stays below 10 m/s, the rate of wheel load reduction of each car is less than the limit of 0.8, and the train operation can be considered safe. When the crosswind speed reaches 15 m/s and the plates are closed, the rate of wheel load reduction of all the cars in the vehicle meet the operational safety standard; however, when the braking plates are opened, the rate of wheel load reduction of the head car exceeds its limit, and that of the middle car increases to 0.765; although this is still within the limit, it offers no safety for train operation. When the crosswind speed is 20 m/s, the rate of wheel load reduction of the head car does not meet the safety standard, regardless of the open/close state of the plate. The head car is therefore a representative for the safety of the whole train when considering the rate of wheel load reduction, and the safe crosswind speed threshold of a train travelling at 350 km/h with an open braking plate is below 10 m/s.

In conclusion, under crosswind, regardless of the open/close state of the braking plates, the derailment coefficient and rate of wheel load reduction of the head car are far greater than those of the other cars. Therefore, the safety indicators of the head car alone can be used to evaluate the safety conditions of the entire train. Under strong crosswinds, it is recommended that the plates located on the head car of the train are never opened.

## 7 Conclusion

The unsteady flow field, aerodynamic performance, and dynamic performance of a train during its braking plate opening process under crosswinds at different speeds were analyzed in this work. The following conclusions were obtained:

- Aerodynamic forces acting on the braking plate during its opening process are transient, and an increase in the crosswind speed leads to increases in both the amplitude and fluctuation of the aerodynamic forces of the plate. When the plate is opened, they show significant fluctuations that are aggravated by crosswind (the lift of the plate is less affected). The aerodynamic forces acting on the upstream plate are relatively large, and those on the downstream plate are reduced.
- Both the aerodynamic forces on each car body and their distribution around the train are significantly affected by crosswind (especially for the head car), and the train aerodynamic performance is directly related to the number of plates.
- Both the derailment coefficient and rate of wheel load reduction of each car are worsened by crosswind, regardless of whether the plate is opened or closed. Both parameters increase with the increase in crosswind speed. The derailment coefficient and rate of wheel load reduction of the head car are always the largest across all cars in the train; hence, the performance of the head car represents the safety threshold of the entire train.

The research herein described studies the impact of the braking plate opening movement on the dynamic performance of a train under crosswind. We believe that this will become an important reference to study the safety of train aerodynamic braking under crosswinds. A solution to reduce the impact of braking plates on train safety performance is proposed. Train

safety performance starts to be compromised when the head car reaches a critical derailment coefficient and rate of wheel load reduction; this will be the focus of our future work. When braking plates are used, the train is subjected to an abrupt braking drag, which affects the comfort inside the train. The influence of the braking plates on the longitudinal dynamics of a train is therefore a key concern that merits further research to improve train safety and comfort.

**Acknowledgements** This study was supported by the National Natural Science Foundation of China (52172359), the Foundation of Maglev Technology Key Laboratory of Railway Industry, Sichuan Science and Technology Program (2020JDTD0012).

**Funding** The funding was provided by Innovative Research Group Project of the National Natural Science Foundation of China (Grant No. 52172359) and Foundation of Maglev Technology Key Laboratory of Railway Industry, Sichuan Science and Technology Program (Grant No. 2020JDTD0012).

**Data availability statement** The data that support the findings of this study are available from the corresponding author, upon reasonable request.

#### Declarations

**Conflict of interest** The authors declare that they have no conflict of interest.

#### References

- Kazumasa, O., Masafumi, Y.: Development of aerodynamic brake of maglev vehicle for emergency use. *Q. Rep. Railw. Tech. Res. Instit.* **37**(2), 60–65 (1989)
- Sawada, K.: Development of magnetically levitated high speed transport system in Japan. *IEEE Trans. Magn.* **32**(4), 2230–2235 (1996)
- Tian, C., Wu, M., Zhu, Y., Fei, W.: Numerical simulation research on the arrangement of the aerodynamic braking plates in the train China. *Railw. Sci.* **33**(3), 100–103 (2012)
- Gao, L., Xi, Y., Fu, Q., Zhu, M., Zhang, J.: Performance analysis of a new type of wind resistance brake mechanism based on fluent and Ansys. *Adv. Mater. Res.* **562–564**, 1099–1102 (2012)
- Tian, C., Wu, M., Fei, W., Huang, Q.: Rule of aerodynamics braking force in longitudinal different position of high-speed train. *J. Tongji Univ. (Natural Science)* **39**(5), 705–709 (2014)
- Gao, L., Xi, L., Wang, G., Zuo, J., Wu, M.: CFD-based study on aerodynamic brake wind-panel forms for high-speed train. *Chin. J. Construct. Mach.* **13**(3), 236–241 (2015)
- Zuo, J., Luo, Z., Chen, Z.: Position control optimization of aerodynamic brake device for high-speed trains. *Chin. J. Mech. Eng.* **27**(2), 287–295 (2014)
- Gao, L., Xi, Y., Wang, G., Zuo, J.: Opening angle rules of the aerodynamic brake panel. *J. Donghua Univ. (English Edition)*. **33**(1), 20–24 (2016)
- Niu, J., Wang, Y., Wu, D., Liu, F.: Comparison of different configurations of aerodynamic braking plate on the flow around a high-speed train. *Eng. Appl. Comput. Fluid Mech.* **14**(1), 655–668 (2020)
- Niu, J., Wang, Y., Zhou, D.: Effect of the outer windshield schemes on aerodynamic characteristics around the car-connecting parts and train aerodynamic performance. *Mech. Syst. Signal Process.* **130**, 1–16 (2019)
- Niu, J., Wang, Y., Liu, F., Li, R.: Aerodynamic behavior of a high-speed train with a braking plate mounted in the region of inter-car gap or uniform-car body: A comparative numerical study. *Proc. Instit. Mech. Eng. Part F J. Rail Rapid Transit.* **235**(7), 815–826 (2021)
- Niu, J., Wang, Y., Liu, F., Chen, Z.: Comparative study on the effect of aerodynamic braking plates mounted at the inter-carriage region of a high-speed train with pantograph and air-conditioning unit for enhanced braking. *J. Wind Eng. Ind. Aerodyn.* **206**, 104360 (2020)
- Niu, J., Wang, Y., Liu, F., Li, R.: Numerical study on the effect of a downstream braking plate on the detailed flow field and unsteady aerodynamic characteristics of an upstream braking plate with or without a crosswind. *Veh. Syst. Dyn.* **59**(5), 657–674 (2021)
- Puharić, M., Linić, S., Matić, D., Lučanin, V.: Determination of braking force of aerodynamic brakes for high-speed trains. *Trans. Famena.* **35**(3), 57–66 (2011)
- Puharić, M., Matić, D., Linić, S., Ristić, S., Lučanin, V.: Determination of braking force on the aerodynamic brake by numerical simulations. *FME Trans.* **42**(2), 106–111 (2014)
- Takami, H.: Development of small-sized aerodynamic brake for high-speed railway. *Trans. Jpn. Soc. Mech. Eng. Ser. B* **79**(803), 1254–1263 (2013)
- Zhai, Y., Niu, J., Wang, Y., Liu, F., Li, R.: Unsteady flow and aerodynamic behavior of high-speed train braking plates with and without crosswinds. *J. Wind Eng. Ind. Aerodyn.* **206**, 104309 (2020)
- Tian, H.: Review of research on high-speed railway aerodynamics in China. *Transport. Saf. Environ.* **1**(1), 1–21 (2019)
- Cheli, F., Ripamonti, F., Rocchi, D., Tomasini, G.I.S.E.L.L.A.: Aerodynamic behavior investigation of the new EMUV250 train to cross wind. *J. Wind Eng. Ind. Aerodyn.* **98**(4–5), 189–201 (2010)
- Li, T., Zhang, J., Zhang, W.: A numerical approach to the interaction between airflow and a high-speed train subjected to crosswind. *J. Zhejiang Univ. SCIENCEA (Appl. Phys. Eng.)* **14**(7), 482–493 (2013)
- Niu, J., Zhou, D., Wang, Y.: Numerical comparison of aerodynamic performance of stationary and moving trains with or without windbreak wall under crosswind. *J. Wind Eng. Ind. Aerodyn.* **182**, 1–15 (2018)
- He, X., Li, H.: Review of aerodynamics of high-speed train-bridge system in crosswinds. *J. Central South Univ.* **27**(4), 1054–1073 (2020)
- Deng, E., Yang, W., He, X., Zhu, Z., Wang, H., Wang, Y., Zhou, L.: Aerodynamic response of high-speed trains under crosswind in a bridge-tunnel section with or without a wind barrier. *J. Wind Eng. Ind. Aerodyn.* **210**, 104502 (2021)

24. Liu, D., Lu, Z., Zhong, M., Cao, T., Chen, D., Xiong, Y.: Measurements of car-body lateral vibration induced by high-speed trains negotiating complex terrain sections under strong wind conditions. *Veh. Syst. Dyn.* **56**(2), 173–189 (2018)
25. Liu, T., Chen, Z., Zhou, X., Zhang, J.: A CFD analysis of the aerodynamics of a high-speed train passing through a windbreak transition under crosswind. *Eng. Appl. Comput. Fluid Mech.* **12**(1), 137–151 (2018)
26. Chen, Z., Liu, T., Yu, M., Chen, G., Chen, M., Guo, Z.: Experimental and numerical research on wind characteristics affected by actual mountain ridges and windbreaks: a case study of the Lanzhou-Xinjiang high-speed railway. *Eng. Appl. Comput. Fluid Mech.* **14**(1), 1385–1403 (2020)
27. Chen, Z., Liu, T., Li, W., Guo, Z., Xia, Y.: Aerodynamic performance and dynamic behaviors of a train passing through an elongated hillock region beside a windbreak under crosswinds and corresponding flow mitigation measures. *J. Wind Eng. Ind. Aerodyn.* **208**, 104434 (2021)
28. Sun, Z., Dai, H., Gao, H., Li, T., Song, C.: Dynamic performance of high-speed train passing windbreak breach under unsteady crosswind. *Veh. Syst. Dyn.* **57**(3), 408–424 (2019)
29. Sun, Z., Dai, H., Hemida, H., Li, T., Huang, C.: Safety of high-speed train passing by windbreak breach with different sizes. *Veh. Syst. Dyn.* **58**(12), 1935–1952 (2020)
30. Wei, L., Zeng, J., Gao, H., Qu, S.: On-board measurement of aerodynamic loads for high-speed trains negotiating transitions in windbreak walls. *J. Wind Eng. Ind. Aerodyn.* **222**, 104923 (2022)
31. Liu, T., Wang, L., Gao, H., Xia, Y., Guo, Z., Li, W., Liu, H.: Research progress on train operation safety in Xinjiang railway under wind environment. *Transport. Saf. Environ.* **4**(2), tda05 (2022)
32. Chen, Z., Ni, Y., Wang, Y., Wang, S., Liu, T.: Mitigating crosswind effect on high-speed trains by active blowing method: a comparative study. *Eng. Appl. Comput. Fluid Mech.* **16**(1), 1064–1081 (2022)
33. BS EN 14067–6: 2010. Railway applications aerodynamics—Part 6: requirements and test procedures for cross wind assessment
34. Borges, R., Carmona, M., Costa, B., Don, W.: An improved weighted essentially non-oscillatory scheme for hyperbolic conservation laws. *J. Comput. Phys.* **227**(6), 3191–3211 (2008)
35. Gritskevich, M.S., Garbaruk, A.V., Schütze, J., Menter, F.R.: Development of DDES and IDDES formulations for the  $k-\omega$  shear stress transport model. *Flow Turbul. Combust.* **88**(3), 431–449 (2012)
36. Shur, M., Spalart, P., Strelets, M., Travin, A.: A hybrid RANS-LES approach with delayed-DES and wall-modelled LES capabilities. *Int. J. Heat Fluid Flow* **29**(6), 1638–1649 (2008)
37. He, K., Su, X., Gao, G., Krajnović, S.: Evaluation of LES, IDDES and URANS for prediction of flow around a streamlined high-speed train. *J. Wind Eng. Ind. Aerodyn.* **223**, 104952 (2022)
38. Wang, S., Bell, J., Burton, D., Herbst, A., Sheridan, J., Thompson, M.: The performance of different turbulence models (URANS, SAS and DES) for predicting high-speed train slipstream. *J. Wind Eng. Ind. Aerodyn.* **165**, 46–57 (2017)
39. Munoz-Paniagua, J., García, J., Lehueur, B.: Evaluation of RANS, SAS and IDDES models for the simulation of the flow around a high-speed train subjected to crosswind. *J. Wind Eng. Ind. Aerodyn.* **171**, 50–66 (2017)
40. Li, T., Hemida, H., Zhang, J., Rashidi, M., Flynn, D.: Comparisons of shear stress transport and detached eddy simulations of the flow around trains. *J. Fluids Eng.* **140**(11), 111108 (2018)
41. Du, J., Liang, X., Li, G., Tian, H., Yang, M.: Numerical simulation of rainwater accumulation and flow characteristics over windshield of high-speed trains. *J. Central South Univ.* **27**(1), 198–209 (2020)
42. Wang, J., Minelli, G., Dong, T., He, K., Krajnović, S.: Impact of the bogies and cavities on the aerodynamic behavior of a high-speed train. An IDDES study. *J. Wind Eng. Ind. Aerodyn.* **207**, 104406 (2020)
43. Guo, Z., Liu, T., Liu, Z., Chen, X., Li, W.: An IDDES study on a train suffering a crosswind with angles of attack on a bridge. *J. Wind Eng. Ind. Aerodyn.* **217**, 104735 (2021)
44. Guo, D., Shang, K., Zhang, Y., Yang, G., Sun, Z.: Influences of affiliated components and train length on the train wind. *Acta Mech. Sin.* **32**(2), 191–205 (2016)
45. Xia, C., Wang, H., Shan, X., Yang, Z., Li, Q.: Effects of ground configurations on the slipstream and near wake of a high-speed train. *J. Wind Eng. Ind. Aerodyn.* **168**, 177–189 (2017)
46. Liang, X., Zhang, X., Chen, G., Li, X.: Effect of the ballast height on the slipstream and wake flow of high-speed train. *J. Wind Eng. Ind. Aerodyn.* **207**, 104404 (2020)
47. Zhang, J., Guo, Z., Han, S., Krajnović, S., Sheridan, J., Gao, G.: An IDDES study of the near-wake flow topology of a simplified heavy vehicle. *Transport. Saf. Environ.* **4**(2), tda015 (2022)
48. Zhou, D., Wu, L., Tan, C., Hu, T.: Study on the effect of dimple position on drag reduction of high-speed maglev train. *Transport. Saf. Environ.* **3**(4), tda027 (2021)
49. Zhang, R.F., Bilige, S.: Bilinear neural network method to obtain the exact analytical solutions of nonlinear partial differential equations and its application to p-g BKP equation. *Nonlinear Dyn.* **95**, 3041–3048 (2019)
50. Zhang, R.F., Li, M.C., Mohammed, A., Zheng, F.C., Lan, Z.Z.: Generalized lump solutions, classical lump solutions and rogue waves of the (2+1)-dimensional Caudrey-Dodd-Gibbon-Kotera-Sawada-like equation. *Appl. Math. Comput.* **403**, 0096–3003 (2021)
51. Neto, J., et al.: Evaluation of the train running safety under crosswinds—A numerical study on the influence of the wind speed and orientation considering the normative Chinese Hat Model. *Int. J. Rail Transport.* **9**(3), 1–28 (2020)
52. Wang, L.H., Huang, A.N., Liu, G.W.: Research on running stability of the rail vehicle based on SIMPACK. *Appl. Mech. Mater.* **2432**(328–328), 589–593 (2013)
53. Di Nino, S., Luongo, A.: Nonlinear dynamics of a base-isolated beam under turbulent wind flow. *Nonlinear Dyn.* **107**, 1529–1544 (2022)
54. Shen, J.L., Wu, X.Y.: Periodic-soliton and periodic-type solutions of the (3+1)-dimensional Boiti–Leon–Manna–Pempinelli equation by using BNNM. *Nonlinear Dyn.* **106**, 831–840 (2021)
55. Zhang, R.F., Li, M.C., Gan, J.Y., Li, Q., Lan, Z.Z.: Novel trial functions and rogue waves of generalized breaking

- soliton equation via bilinear neural network method. *Chaos, Solitons Fractals* **154**(ISSN), 0960–1779 (2022)
56. Wu, H., Zhou, Z.J.: Study on aerodynamic characteristics and running safety of two high-speed trains passing each other under crosswinds based on computer simulation technologies. *J. Vibroeng.* **19**(8), 6328–6345 (2017)
57. Yan, J., et al.: Influence of posture change on train running safety under crosswind[J]. *Appl. Sci.* **11**(13), 6067–6067 (2021)
58. Jun, X., Qingyuan, Z.: A study on mechanical mechanism of train derailment and preventive measures for derailment. *Veh. Syst. Dyn.* **43**(2), 121–147 (2005)
59. Zhai, W., Cai, C., Guo, S.: Coupling model of vertical and lateral vehicle/track interactions. *Veh. Syst. Dyn.* **26**(1), 61–79 (1996)
60. Wang, K., Huang, C., Zhai, W., Liu, P., Wang, S.: Progress on wheel-rail dynamic performance of railway curve negotiation. *J. Traffic Transport. Eng. (English edition)*. **1**(3), 209–220 (2014)
61. TB 10621–2009, Code for Design of High-Speed Railway.
62. Chen, Z.W., Liu, T.H., Yan, C.G., et al.: Numerical simulation and comparison of the slip-streams of trains with different nose lengths under crosswind. *J. Wind Eng. Ind. Aerodyn.* **190**, 256–272 (2019)

**Publisher's Note** Springer Nature remains neutral with regard to jurisdictional claims in published maps and institutional affiliations.

Springer Nature or its licensor (e.g. a society or other partner) holds exclusive rights to this article under a publishing agreement with the author(s) or other rightsholder(s); author self-archiving of the accepted manuscript version of this article is solely governed by the terms of such publishing agreement and applicable law.